

Robust Triboelectric Nanogenerator Achieved by Centrifugal Force Induced Automatic Working Mode Transition

Jie Chen, Hengyu Guo,* Chenguo Hu,* and Zhong Lin Wang*

Material abrasion in contact-based freestanding mode-triboelectric nanogenerators (FS-TENGs) seriously deteriorates device mechanical durability and electrical stability, which causes TENGs to be only applicable in the harvesting of mechanical energy at low-frequency. Here, a wide-frequency and ultra-robust rotational TENG is reported that is composed of a built-in traction rope structure and capable of transforming from contact mode to non-contact mode automatically as driven by the centrifugal force. With optimizing the fixed x and y position on slider and center shaft, respectively, the mode transition threshold speed can be reduced to 225 rpm. Additionally, the automatic working mode transition TENG exhibits excellent electrical stability, which can maintain 90% electric output after over 24 h of continuous operation, while the contact and non-contact mode TENGs only retain 30% and 2% output, respectively. The high stability and large output density ensure its usage in the fast and effective charging of commercial capacitors or electronics. This work provides a prospective strategy for rotational TENGs to extend the frequency operation region and mechanical durability for practical applications.

sensing devices.^[8–14] Typically, TENG are divided into four basic working modes, contact-separation mode,^[15] single electrode mode,^[16] in-plane sliding mode,^[17] and free-standing mode (FS),^[18] among which FS-TENG exhibits high energy conversion efficiency and is the easiest way to achieve the scavenging of regular motion such as rotation through advanced structure design.^[19–21]

Compared with the traditional electromagnetic generator, TENG has an overwhelming dominance in the low-frequency mechanical energy region,^[22–26] but at high frequency, the heat generated by sliding friction cannot be released in time, and the corresponding mechanical abrasion will lead to a serious decline in the output performance of TENG.^[27–31] For practical applications, FS-TENG inevitably needs to operate at medium and even high-frequency regions, especially in

scavenging the mechanical energy of airflow,^[32–34] water flow,^[35] rotational tire^[36] etc. Therefore, reducing mechanical wear at medium–high frequency is an important kernel to broaden the applications of FS-TENG. In this case, one of the solutions is to develop a non-contact structure to avoid direct friction between tribo-materials.^[37] However, the charges preserved on the surface of dielectric tribo-layers will gradually dissipate, leading to a decline in the electric output.^[38] This means the operation of non-contact mode devices has to be frequently interrupted for surface charge replenishment. Given all this, the development of TENG that can work in contact mode to replenish tribo-charges at low frequency and automatically switch non-contact mode at high frequency would be the most effective strategy to maximize mechanical durability and expand working frequency.

In this work, a rotational TENG enabling the automatic mode transition (AMT) between contact and non-contact mode is proposed with a built-in traction rope structure. From both theoretical analysis and experimental demonstration, AMT-TENG can transform working mode automatically under the function of centrifugal force and has the advantage of wide-frequency working region and ultra-robustness in mechanical energy conversion. Also, an experimental study about the influence of mode transition speed on fixed position x and y indicates that the threshold speed is tunable and can be reduced to 225 rpm by cutting x down to 4.5 mm. In contrast, AMT-TENG exhibits excellent electrical stability, which can maintain 90% of electric output over a continuous operation of 24 h, while contact and non-contact TENG only retain 30% and 2% of output, respectively. Finally, to demonstrate the capability of


1. Introduction

In recent years, originating from Maxwell's displacement current,^[1,2] triboelectric nanogenerator (TENG) has demonstrated its prospective applications of building self-powered sensor systems in the era of the internet of things through the utilization of distributed mechanical energy from ambient environment.^[3–7] By now, TENGs have been proven to be the most efficient way to convert mechanical movements to electricity as energy and

J. Chen, Prof. H. Guo, Prof. Z. L. Wang
School of Materials Science and Engineering
Georgia Institute of Technology
Atlanta, GA 30332-0245, USA
E-mail: hguo62@gatech.edu; cqphysicsghy@126.com;
zhong.wang@mse.gatech.edu

J. Chen, Prof. H. Guo, Prof. C. Hu
Department of Applied Physics
State Key Laboratory of Power Transmission Equipment and System
Security and New Technology
Chongqing University
Chongqing 400044, P. R. China
E-mail: hucg@cqu.edu.cn

Prof. H. Guo, Prof. Z. L. Wang
College of Nanoscience and Technology
University of Chinese Academy of Sciences
Beijing 100049, P. R. China

 The ORCID identification number(s) for the author(s) of this article can be found under <https://doi.org/10.1002/aenm.202000886>.

DOI: 10.1002/aenm.202000886

AMT-TENG working at high frequency, 33 m s^{-1} wind speed (level of 12 typhoon) was employed as the driver. An AC output flows through the external power management circuit first and then charges the three parallel-connected hygro-thermographs and three types of light bulbs. This work provides a prospective strategy of TENG to extend the frequency operation region and mechanical durability for practical applications.

2. Results and Discussion

2.1. Structure Design and Working Principle of AMT-TENG

TENG is the most powerful technology to harvest ambient mechanical energy^[39–41] in the $<5 \text{ Hz}$ trigger frequency region.^[23] However, for some practical applications that require energy converters operating at high frequency, such as scavenging mechanical energy of airflow, water flow, and rotational tires, TENG inevitably appears tribo-material wear out in short-term and electrical output struggling to external stimuli. Thus, broadening working frequency and maximizing mechanical durability are still challenging for further improving the

effectiveness of TENG. In this context, we presented a strategy for realizing AMT-TENG enabled by utilizing centrifugal force in a rotational motion to expand the working frequency range and enhance the mechanical durability.

The basic configuration of this designed AMT-TENG is schematically illustrated in **Figure 1a**, consisting of three coaxially mounted components, namely, rotator, stationary electrode, and driving wheel. For the rotator, it includes four sliders and each slider connects with the central shaft by two traction ropes. The same-shaped flexible polyurethane (PU) film attached to the slider bottom to serve as the freestanding tribo-layer. In addition, an acrylic baffle is utilized to restrict the maximum vertical separation distance between the slider and electrode. Four round magnets with the same pole embedded in the back of acrylic baffle cooperate with other four magnets with opposite pole arranged on the drive wheel to induce an attractive force to ensure that the slider rotates in sync with the driving wheel. The stationary part is composed of two separate copper films with complementary four-segment shapes deposited on a round acrylic disk, which acts as the two stationary electrodes. And fluorinated ethylene propylene (FEP) film is employed for fully covering the two stationary electrodes to work as another tribo-layer. Insets 1 and 2

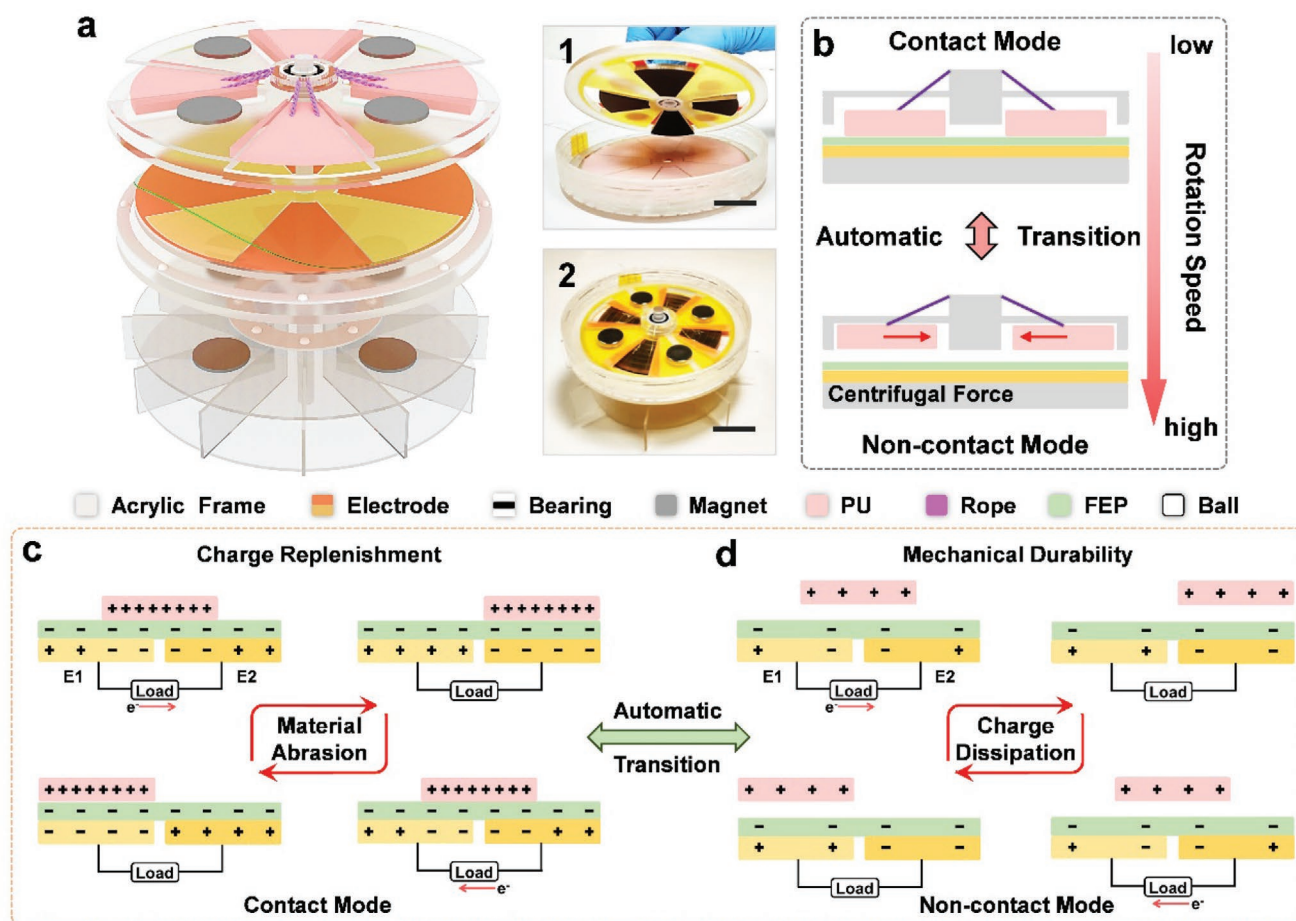


Figure 1. Schematic illustration of the AMT-TENG. a) Hierarchical structure diagram of the rotational AMT-TENG. Inset 1 is the photograph showing the electrode and rotator part. Inset 2 demonstrates the whole device image (scale bar: 3 cm). b) Illustration of the automatic working mode transition between contact mode and non-contact mode triggered by the speed-resolved variation in centrifugal force in a circular motion. c, d) General working principle, drawbacks, and advantages of the contact and non-contact freestanding mode TENG.

show the corresponding digital photographs of the internal structure and whole device. In brief, the automatic working mode transition between contact and non-contact mode is obtained by the centrifugal force generated in rotational motion. At low speeds, the slider stays in full contact with the electrode, while at high speeds, the increased centrifugal force brings slider separating from bottom electrode. The automatic working mode transition is schematically illustrated in Figure 1b and dynamically recorded in Video S1, Supporting Information. The detailed device fabrication process is depicted in the Section 4.

When the freestanding TENG operates in contact mode, the sliding friction between PU and FEP generates tribo-charges on both surfaces due to the triboelectrification effect.^[5] Meanwhile, the periodical approach to the electrodes by PU drives electrons to flow back and forth between two electrodes caused by the electrostatic induction. Although TENG in this mode can produce the highest instantaneous output power owing to the most effective contact electrification,^[42] the severe material abrasion largely limits the long-term mechanical durability, especially in high frequency (Figure 1c). In non-contact mode, electricity can be generated by swing PU between the two electrodes without direct contact. And output power depends on the preserved time

of tribo-charges on dielectric surfaces. The gradual dissipation of surface charges certainly leads to the drop of electric output, further bringing in the unstable electrical performance (Figure 1d). To address this concern, it is better to set TENG work in the non-contact mode in most of working processes to minimize mechanical wear, and can also automatically shift into contact mode intermittently for charge replenishing to retain the electrical stability. Thus, using the built-in traction rope structure, the AMT-TENG capacitated by the centrifugal force can be obtained for achieving the wide-frequency and ultra-robust characteristics.

2.2. Influence Factors on Working Mode Transition

To demonstrate the features of this mode transition strategy, we first establish a simplified model for the built-in rope structure to simulate the slider's force condition, as induced by changing the rotational speed. In this model, we hypothesized that the slider's mass is evenly distributed and its barycenter coincides with the geometrical center (with a length l and thickness of t). There are two side views that briefly show force analysis of the final non-contact state (Figure 2a). In the first case, the traction

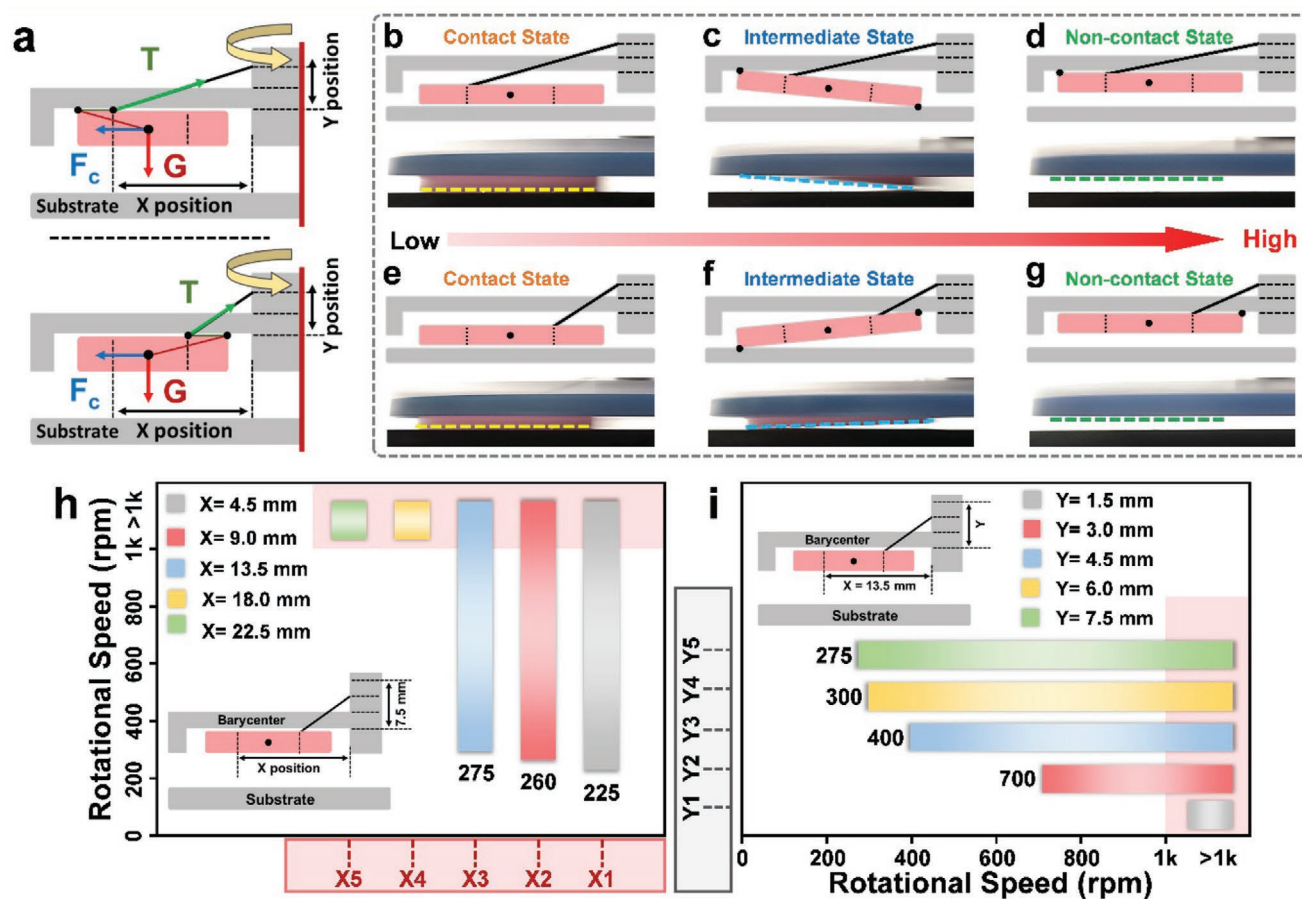


Figure 2. Influence of structural parameters on the working mode transition. a) Force analysis of two typical modes with the point fixing outside and inside of the barycenter along the horizontal direction on the slider. b–g) Schematic diagram and corresponding digital photographs of the contact state, intermediate transition state, and fully non-contact state during the increased rotation speed process in two typical modes. h) Influence of horizontal (x) position when fixed vertical height as 7.5 mm and i) vertical (y) position when fixed horizontal location as 13.5 mm on the threshold mode-transition rotation speed (when slider getting fully separated), respectively.

rope is fixed outside of the barycenter ($l/2 < x < l$), when the device starts to work under an external triggering such as electro-motor, the moving part slides against the bottom substrate in contact to form a circular motion in the x - z plane (Figure 2b). And then, the centrifugal force that is proportional to the square of angular velocity rapidly increases in the speed up rotation process, which makes the tension on rope rise and further causes the slider to rotate clockwise around the left vertex thus form an oblique intermediate state (Figure 2c). As long as the velocity continues to increase, the baffle and rope will base the left vertex to overcome the unbalanced moment, finally, pulls the slider up completely and keep it parallel to the substrate at high speed (Figure 2d). At this moment, the force balance condition in x -axis and moment equilibrium should satisfy the following equations

$$T \cos \theta = F_c \quad (1)$$

$$(l-x)T \sin \theta = \frac{t}{2} F_c + \frac{l}{2} G \left(\frac{l}{2} < x < l \right) \quad (2)$$

where G is the gravity force of the slider, T stands for the tension on the rope, θ is the angle between the rope and x -axis. F_c is the centrifugal force, which depends on the angular velocity ω , shown as follows

$$F_c = m \omega^2 \left(\frac{l}{2} + r \right) \quad (3)$$

In the second case, the fixed point on the slider lies inside of the barycenter ($0 < x < l/2$), its working condition at low speed is consistent with the former (Figure 2e). The only difference is that the slider will rotate counterclockwise around the right vertex to come into being the oblique intermediate state, in the process of speed raising (Figure 2f). The moment at the final non-contact state can be expressed as

$$xT \sin \theta + \frac{t}{2} F_c = \frac{l}{2} G \left(0 < x < \frac{l}{2} \right) \quad (4)$$

Photographs corresponding to the contact state, intermediate state, and non-contact state of these two cases are shown below their respective diagrams (Figure 2), indicating that the experimental results are in line with expectations. Based on the above analysis, the critical angular velocity to achieve mode transition between contact state and non-contact state could be calculated by

$$\omega_{\frac{l}{2} < x < l} = \sqrt{\frac{gl}{\frac{l}{2} + r}} \times \sqrt{\frac{1}{2\gamma \left(\frac{l+r}{x+r} - 1 \right) - t}} \quad (5)$$

$$\omega_{0 < x < \frac{l}{2}} = \sqrt{\frac{gl}{\frac{l}{2} + r}} \times \sqrt{\frac{1}{2\gamma \left(1 - \frac{r}{r+x} \right) + t}} \quad (6)$$

Since g , l , r , t are constant, ω is just a function of the fixed point on the slider (x) and center shaft (y), in which ω and y are approximately inverse to each other. The detailed calculation is presented in Supporting Information and the theoretical curves are plotted in Figure S2, Supporting Information. To verify the theoretical analysis results, we experimentally tested x and y impact on the speed of working mode transition between

contact and non-contact state, shown in Figure 2h,i. By shorting the fixed point distance from 22.5 to 4.5 mm on the x -axis, the mode transition's speed can be depressed to 225 rpm. Also, an obvious decrease on mode transition speed is observed by increasing the fixed point distance from 1.5 to 7.5 mm on the y -axis. Speed-dependent variation in contact states of each slider with different fixed points on the x and y -axis are presented in Figures S3 and S4, Supporting Information, which snapshots in the yellow dotted box reveal the threshold speed at each fixed position that contact mode transfers to a non-contact state. From the influence of x and y , a smaller fixed distance on slider or a larger fixed distance on the center shaft is preferred in structure design for lowering critical speed of mode transition, so that, the AMT-TENG enters non-contact mode at most of the time, avoiding serious friction at medium and high frequency.

2.3. Performance of AMT-TENG

After demonstrating that the contact state can be converted into non-contact mode by the built-in traction rope structure, we conceived a rotational freestanding TENG based on this mode transition strategy to develop the possibility of FS-TENG working at high frequency without sacrificing electrical output. The open-circuit voltage (V_{oc}) and short-circuit transferred charge (Q_{sc}) of AMT-TENG with the optimized x and y position were measured at low, medium, and high speeds. As shown in Figure 3a, both V_{oc} and Q_{sc} stay at the level around 260 V and 98 nC in the contact state. There is only a minor enhanced trend of V_{oc} and Q_{sc} when the device speeds up, probably because of tribo-charges accumulated in the freestanding layer. However, V_{oc} and Q_{sc} have a different trend from those of contact state since the friction area becomes inefficient in a partial separate state, presenting a bit reduction with a continuous increase in rotational speed. It is worth noting that V_{oc} and Q_{sc} decline sharply at the moment of mode transition, and the decrement can be optimized by reducing the separated gap distance. After that, the device goes into a non-contact mode. The photographs of the three stages are presented in the Insets of Figure 3a. For a comprehensive characterization of the demonstrated AMT-TENG, we further compared the electric performances of contact-mode, non-contact mode TENG, and AMT-TENG. The speed-dependent variation of measured Q_{sc} from three equivalent devices was recorded, as shown in Figure 3b. With the increase in working speed from 100 to 800 rpm, Q_{sc} of contact and non-contact mode TENGs retain stable values about 99 nC (black) and 62 nC (red), respectively. While for AMT-TENG, the amplitude of Q_{sc} lowers down from 97 to 65 nC during the rotational speed raising process, eventually, mode transition between contact mode and non-contact occurs at 550 rpm (orange). Note that the speed to trigger a transformation of non-contact mode into contact mode is 350 rpm when the rotational speed falls back to 100 rpm (green). There is a notable speed difference for the mode transition, which results from plenty of charges accumulated to freestanding layer by contact triboelectrification, causing a bigger tensile force needed to overcome greater electrostatic adsorption thus to obtain the mode transition in the speed-up process. The measured Q_{sc} curves of as-fabricated AMT-TENG with rotational speed first going up to 800 rpm and then falling back to 100 rpm, are plotted in

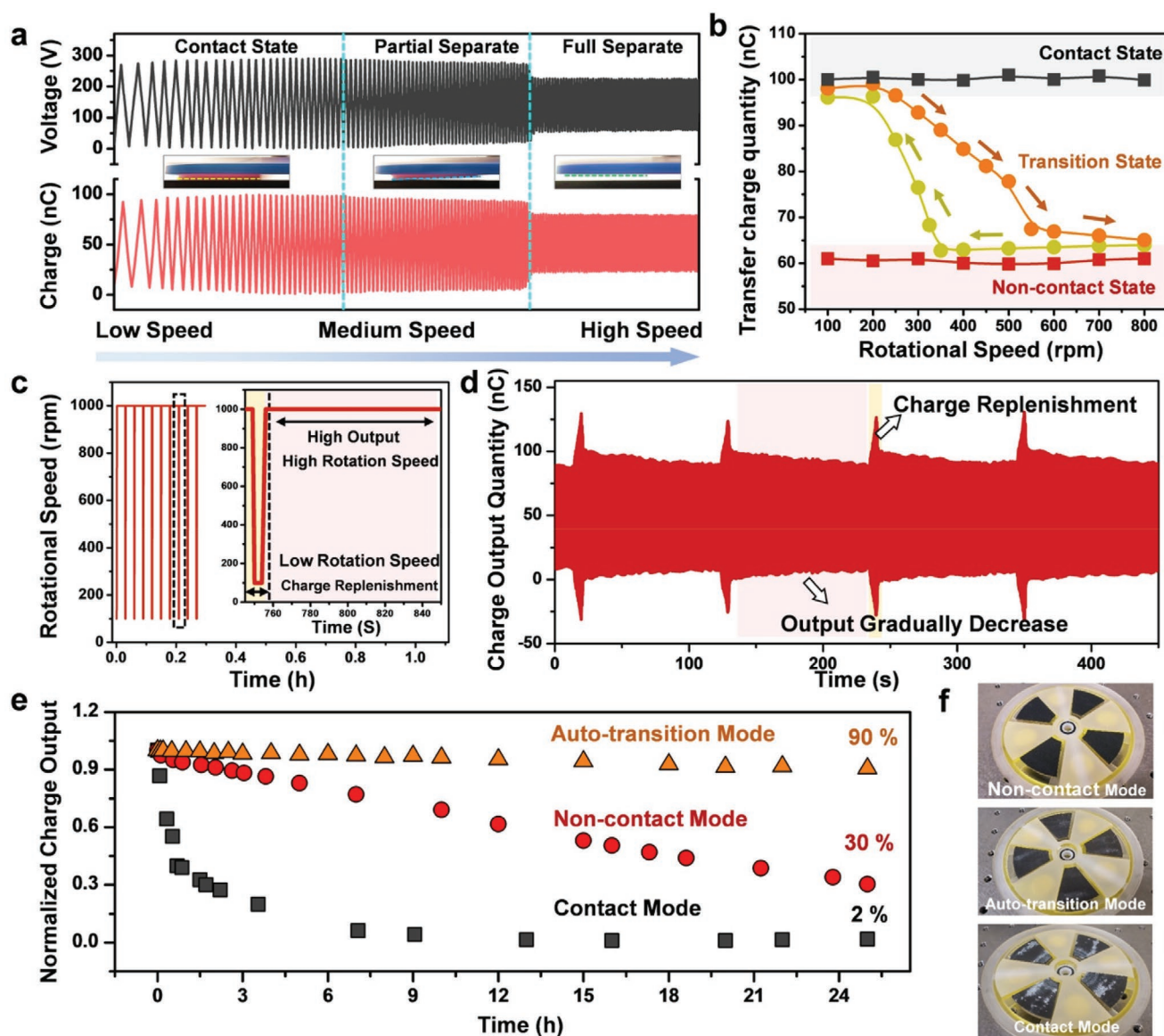


Figure 3. Electric performance and long-term durability of AMT-TENG. a) Open-circuit voltage and short-circuit transferred charge of AMT-TENG with the continuous increase in rotation speed. b) Transferred charge output of contact FS-TENG, AMT-TENG, and non-contact FS-TENG under various rotation speeds. c) Function of rotation speed on time (100 rpm stay for 5 s and 1000 rpm stay for 100 s) generated by a programmed controlled electric motor for long-term durability measurement. d) Transferred charge output of AMT-TENG driven by the electric motor. e) Long-term durability of contact mode, auto-transition mode, and non-contact mode TENG. f) Comparison of the material abrasion for three modes TENG after 24 h of continuous testing.

Figures S5 and S6, Supporting Information. Therefore, the contact mode and non-contact mode can be switched to each other automatically by altering the working speed.

With this capability of mode transition by working speed variation, if the charges can be replenished to freestanding layer in time, AMT-TENG will be able to operate at high frequency and maintain relatively stable output for a long time. Thus, a time-dependent variation in rotational speed provided by a programmed electric motor was employed to drive AMT-TENG first working at 100 rpm for 5 s, and then continuously keeps at 1000 rpm for 100 s (Figure 3c). Based on this periodic motion, the measured Q_{sc} of AMT-TENG is presented

in Figure 3d, showing that the magnitude of Q_{sc} dramatically increases once AMT-TENG rotates at 100 rpm, then stays relatively stable at a lower level with the device continuously speeds up to 1000 rpm. This enhanced electrical stability can be ascribed to lots of charges replenished by contact electrification, which prevents the fast decay in output when the device enters non-contact mode at high frequency. We also examined the long-term durability of AMT-TENG for more than 24 h. The normalized charge output of our device compared with that of contact and non-contact TENG suggests that, AMT-TENG demonstrates excellent electric stability which can maintain 90% electric output, while the other two TENGs maintain only

30% and 2% electric output, respectively (Figure 3e). Compared with the previous reported mode transition works, our designed device not only shows good stability, but also has a higher integration (Table S1, Supporting Information).^[28,43] Combination with the three optical images of material abrasion after long-term durability test, mechanical wear of AMT-TENG is negligible compared to that of contact mode TENG. From all the above results, our device not only can operate well instead of being severely worn out at high frequencies but also takes advantage of the fact that contact-mode TENG accumulates large amounts of charge at low frequency, which largely extends the working frequency region and stabilizes the electrical performance. Thus, based on an architecture that comprises a traction rope, the speed-dependent variation in the centrifugal

force induces an automatic transformation between contact and non-contact mode of rotational TENG, displaying numerous advantages including much higher stability and durability, and much smaller deterioration in performance.

2.4. Application Demonstrations of AMT-TENG

To explore the capability of AMT-TENG for high-frequency mechanical energy harvesting as a practical power, we designed a fully enclosed waterproofing platform additional with a driven wheel and acrylic walls to convert airflow into rotational motion and make sure the device works long-time in a humid environment. Figure 4a shows the AMT-TENG

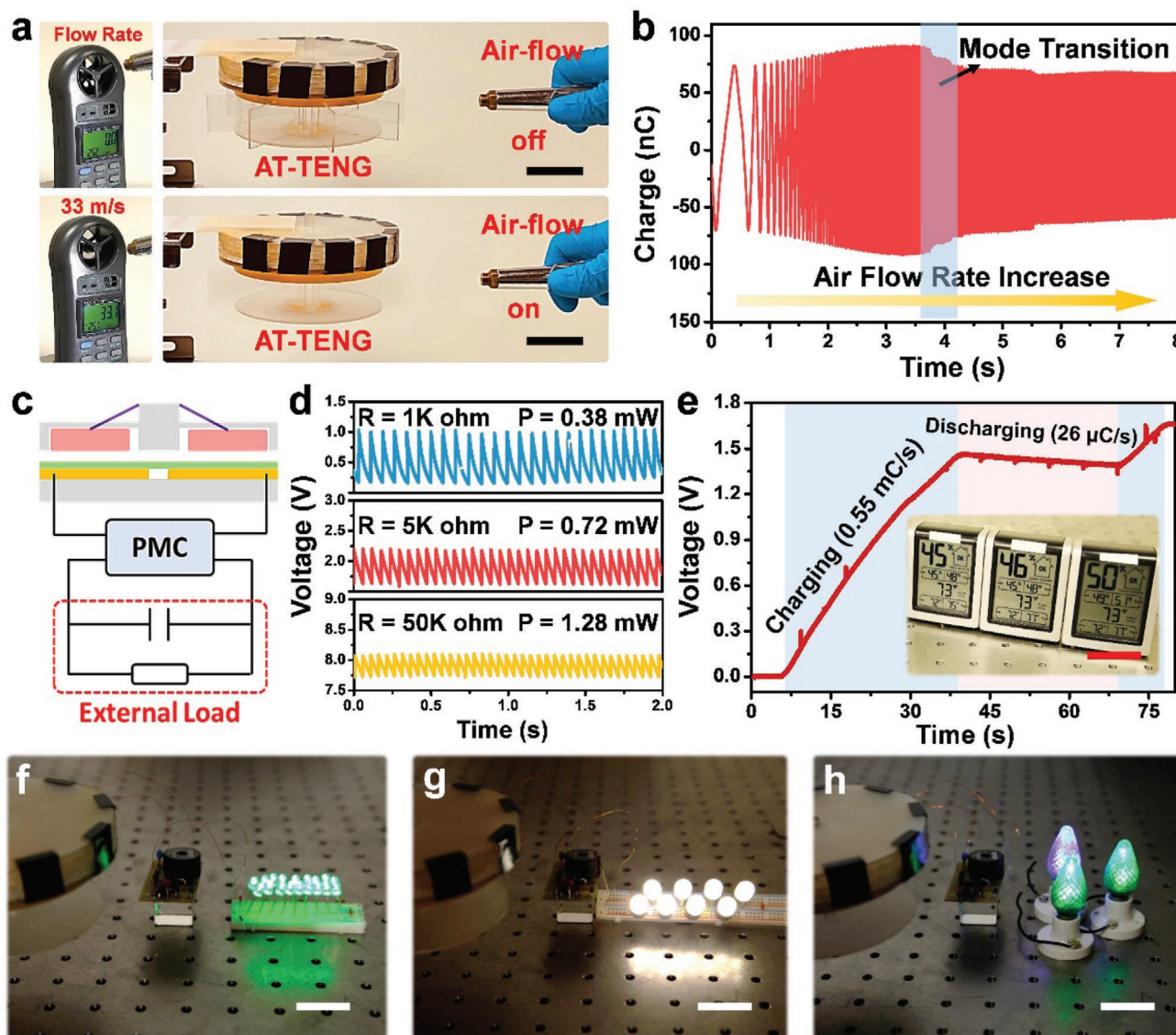


Figure 4. Demonstrations of the AMT-TENG as a practical power source. a) Digital photographs of the AMT-TENG driven by airflow energy (scale bar: 4 cm). b) Output charge of AMT-TENG with increasing the airflow rate. c) Schematic diagram of AMT-TENG with a power management circuit to work as a DC power source. d) Output voltage and calculated average power of AMT-TENG under 1, 5, and 50 k Ω external loads. e) Charging curve of a 10 mF commercial capacitor while powering three parallel-connected hydro-thermographs, driven by AMT-TENG. Inset is the photograph showing the room temperature and humidity (scale bar: 3 cm). f–h) Three types of bulbs lighted by AMT-TENG (scale bar: 2 cm).

from “off” state to “on” state under the airflow of 33 m s^{-1} . By adjusting the airflow rate, we can precisely control the mode transition for enhanced on-demand output, indicating that efficient energy generation from a wide range of frequency can be obtained based on this structure (Figure 4b). For most of the electronics, it is needed to be powered by a DC signal, thus, the AC output from AMT-TENG is applied to both ends of a commercial capacitor (10 mF) via a power management circuit, in which the generated electricity is first stored in capacitor and then utilized to charge electronics (Figure 4c). The detailed circuit diagram of power management is plotted in Figure S7, Supporting Information. According to measured voltages loaded on 1, 5, and 50 k Ω resistors, we calculated their average output power with the value of 0.38, 0.72, and 1.28 mW, respectively, presented in Figure 4d. Similarly, such a platform can serve as a power supply for other commercial electronics. From the measured charging curve in Figure 4e, it can be found that three parallel-connected thermo-hygrometers are charged from 0 to 1.45 V in $\approx 38 \text{ s}$ with the 0.55 mC s^{-1} charging rate, under the power supply of AMT-TENG driven by air-flow. At this time, thermo-hygrometers start to detect room temperature and humidity with the discharging rate of $26 \text{ }\mu\text{C s}^{-1}$, which is much less than the charging rate. The whole working process of the thermo-hygrometer is recorded in Video S2, Supporting Information. In addition, three type bulbs are also successfully lit up by the energy generated from AMT-TENG after rectification. The snapshots and movies are shown in Figure 4f–h and Videos S3–S5, Supporting Information. This new mode transition strategy allows AMT-TENG to operate in high frequency ignoring charge dissipation and largely expands the mechanical durability.

3. Conclusion

In summary, this paper demonstrates an auto-mode-transition strategy for rotational TENG utilizing centrifugal force by the built-in traction rope structure, and achieves wide-frequency and ultra-robustness properties in mechanical energy conversion. The capability of our device to automatically transform the working mode between contact and non-contact mode by adjusting rotational speed has been elucidated with the conjunction of schematic illustrations, theoretical analysis, as well as experimental examinations. Also, an experimental study on the influence of mode transition speed in the fixed position x and y indicates that the threshold speed is tunable and can be reduced to 225 rpm by cutting x down to 4.5 mm. In contrast, AMT-TENG exhibits much small and slow deterioration in output performance, which can maintain 90% on electric output over a continuous operation of 24 h, while the TENG that works in contact and non-contact mode only retain 30% and 2% electrical output, respectively. The high stability and large output energy density ensure its usage in the fast and effective charging of commercial capacitors or electronics. Finally, based on the excellent electrical stability, AMT-TENG could be employed as a power source to charge three parallel-connected hygrothermographs and three types of light bulbs.

This work provides a prospective strategy of TENG to extend the frequency operation region and mechanical durability for practical applications.

4. Experimental Section

Fabrication of the AMT-TENG Components: AMT-TENG mainly composed of three coaxially mounted components, rotator, stationary electrode, and driving wheel. For the rotator, a 2 mm thick PU sheet was shaped by a laser cutter to form a 1/8 annulus (inner diameter: 25 mm, external diameter: 80 mm), and then was stuck to one side of an acrylic substrate with the same configuration (thickness: 3 mm), acting as the slider. Four well-prepared sliders were confined to an acrylic frame with a certain gap on around for movement. Four permanent disc magnets (thickness: 3 mm, diameter: 15 mm) with the same magnetic pole were evenly arranged and fixed on an acrylic disk (thickness: 1.5 mm, diameter: 100 mm) around the center. This magnet disk was fastened on top of the frame as a baffle for limiting the maximum vertical distance between the slider and electrode. For the stationary electrode, an acrylic sheet with a thickness of 3 mm was shaped to a hollow disk (inner diameter: 6 mm, external diameter: 100 mm). Then, electrodes with complementary patterns had been deposited onto the disk by pulsed vapor deposition. Two lead wires were connected respectively to the two sets of electrodes. A commercial FEP film (50 μm) was aligned onto the electrodes as a tribo-layer. For the driving wheel, it contains two hollow disks and eight rectangle blades, which were installed underside of the electrode for forming a driven wheel to convert airflow into a rotational motion. And the top disk was fixed with four magnets of which poles were opposite of the magnets on the rotator.

Assemblage of AMT-TENG: All the parts were joined-up by a central shaft (diameter: 6 mm), and two bearings on the central shaft were used for connecting the rotator and driving wheel, respectively. Each slider was connected to the central shaft by two ropes. Combined with the attractive force from magnet groups, the rotator could move synchronously with the driving wheel. In order to reduce the resistance, two sets of lubricating balls were employed to separate the rotator, stator, and driving wheel.

Electrical Measurement: The device was first driven by an electro-motor, in which contact states between the slider and electrode were recorded by a high-speed camera. The electrical performances of AMT-TENG were measured by a voltage amplifier (Keithley 6514). In application demonstration, AMT-TENG was driven by airflow and the corresponding air rate was characterized by an aerometer.

Supporting Information

Supporting Information is available from the Wiley Online Library or from the author.

Acknowledgements

The research was supported by the National Key R&D Project from Minister of Science and Technology (2016YFA0202704), the Fundamental Research Funds for the Central Universities (Grant No. 2019CDXZWL001, 2018CDJDWL0011), and the National Natural Science Foundation of China (51572040).

Conflict of Interest

The authors declare no conflict of interest.

Keywords

energy harvesting, mode transition, triboelectric nanogenerators

Received: March 8, 2020

Revised: April 10, 2020

Published online:

-
- [1] Z. L. Wang, *Mater. Today* **2017**, *20*, 74.
 [2] Z. L. Wang, *Nano Energy* **2020**, *68*, 104272.
 [3] Y. Hu, Z. L. Wang, *Nano Energy* **2015**, *14*, 3.
 [4] R. Hinchet, W. Seung, S. W. Kim, *ChemSusChem* **2015**, *8*, 2327.
 [5] S. Pan, Z. Zhang, *Friction* **2019**, *7*, 2.
 [6] A. E. Wang, P. S. Gil, M. Holonga, Z. Yavuz, H. T. Baytekin, R. M. Sankaran, D. J. Lacks, *Phys. Rev. Mater.* **2017**, *1*, 035605.
 [7] Z. L. Wang, T. Jiang, L. Xu, *Nano Energy* **2017**, *39*, 9.
 [8] H. Guo, J. Chen, L. Tian, Q. Leng, Y. Xi, C. Hu, *ACS Appl. Mater. Interfaces* **2014**, *6*, 17184.
 [9] H. Guo, X. He, J. Zhong, Q. Zhong, Q. Leng, C. Hu, J. Chen, L. Tian, Y. Xi, J. Zhou, *J. Mater. Chem. A* **2014**, *2*, 2079.
 [10] X. Liu, A. Yu, A. Qin, J. Zhai, *Adv. Mater. Technol.* **2019**, *4*, 1900608.
 [11] J. Wang, C. Wu, Y. Dai, Z. Zhao, A. Wang, T. Zhang, Z. L. Wang, *Nat. Commun.* **2017**, *8*, 88.
 [12] L. Xu, T. Jiang, P. Lin, J. J. Shao, C. He, W. Zhong, X. Y. Chen, Z. L. Wang, *ACS Nano* **2018**, *12*, 1849.
 [13] D. Anaya, T. He, C. Lee, M. Yuçe, *Nano Energy* **2020**, *72*, 104675.
 [14] C. Qiu, F. Wu, C. Lee, M. Yuçe, *Nano Energy* **2020**, *70*, 104456.
 [15] S. Niu, S. Wang, L. Lin, Y. Liu, Y. S. Zhou, Y. Hu, Z. L. Wang, *Energy Environ. Sci.* **2013**, *6*, 3576.
 [16] S. W. Chen, X. Cao, N. Wang, L. Ma, H. R. Zhu, M. Willander, Y. Jie, Z. L. Wang, *Adv. Energy Mater.* **2017**, *7*, 1601255.
 [17] D. Liu, X. Yin, H. Guo, L. Zhou, X. Li, C. Zhang, J. Wang, Z. L. Wang, *Sci. Adv.* **2019**, *5*, eaav6437.
 [18] M. Kang, T. Y. Kim, W. Seung, J. H. Han, S. W. Kim, *Micromachines* **2019**, *10*, 9.
 [19] H. Qin, G. Gu, W. Shang, H. Luo, W. Zhang, P. Cui, B. Zhang, J. Guo, G. Cheng, Z. Du, *Nano Energy* **2020**, *68*, 104372.
 [20] T. Jiang, X. Chen, C. B. Han, W. Tang, Z. L. Wang, *Adv. Funct. Mater.* **2015**, *25*, 2928.
 [21] Y. Xie, S. Wang, S. Niu, L. Lin, Q. Jing, J. Yang, Z. Wu, Z. L. Wang, *Adv. Mater.* **2014**, *26*, 6599.
 [22] S. Chen, N. Wu, L. Ma, S. Lin, F. Yuan, Z. Xu, W. Li, B. Wang, J. Zhou, *ACS Appl. Mater. Interfaces* **2018**, *10*, 3660.
 [23] Y. Zi, H. Guo, Z. Wen, M. H. Yeh, C. Hu, Z. L. Wang, *ACS Nano* **2016**, *10*, 4797.
 [24] Z. Wen, H. Guo, Y. Zi, M. H. Yeh, X. Wang, J. Deng, J. Wang, S. Li, C. Hu, L. Zhu, Z. L. Wang, *ACS Nano* **2016**, *10*, 6526.
 [25] H. Yang, Y. Pang, T. Bu, W. Liu, J. Luo, D. Jiang, C. Zhang, Z. L. Wang, *Nat. Commun.* **2019**, *10*, 2309.
 [26] X. Pu, H. Guo, J. Chen, X. Wang, Y. Xi, C. Hu, Z. L. Wang, *Sci. Adv.* **2017**, *3*, e1700694.
 [27] X. Du, N. Li, Y. Liu, J. Wang, Z. Yuan, Y. Yin, R. Cao, S. Zhao, B. Wang, Z. L. Wang, C. Li, *Nano Res.* **2018**, *11*, 2862.
 [28] Z. Lin, B. Zhang, H. Zou, Z. Wu, H. Guo, Y. Zhang, J. Yang, Z. L. Wang, *Nano Energy* **2020**, *68*, 104378.
 [29] W. Xu, M.-C. Wong, J. Hao, *Nano Energy* **2019**, *55*, 203.
 [30] H. Shi, Z. Liu, X. Mei, *Energies* **2019**, *13*, 86.
 [31] C. X. Lu, C. B. Han, G. Q. Gu, J. Chen, Z. W. Yang, T. Jiang, C. He, Z. L. Wang, *Adv. Eng. Mater.* **2017**, *19*, 1700275.
 [32] B. Chen, Y. Yang, Z. L. Wang, *Adv. Energy Mater.* **2018**, *8*, 1702649.
 [33] C. Y. Chen, C. Y. Tsai, M. H. Xu, C. T. Wu, C. Y. Huang, T. H. Lee, Y. K. Fuh, *eXPRESS Polym. Lett.* **2019**, *13*, 533.
 [34] X. Ren, H. Fan, C. Wang, J. Ma, N. Zhao, *Smart Mater. Struct.* **2018**, *27*, 065016.
 [35] H. Shao, P. Cheng, R. Chen, L. Xie, N. Sun, Q. Shen, X. Chen, Q. Zhu, Y. Zhang, Y. Liu, Z. Wen, X. Sun, *Nano-Micro Lett.* **2018**, *10*, 54.
 [36] L. Jin, B. Zhang, L. Zhang, W. Yang, *Nano Energy* **2019**, *66*, 104086.
 [37] U. Shaislamov, Y. Kim, W. S. Kim, H. Jeong, H.-J. Lee, W. Chun, *Int. J. Energy Res.* **2017**, *41*, 1412.
 [38] T. Jiang, X. Chen, K. Yang, C. Han, W. Tang, Z. L. Wang, *Nano Res.* **2016**, *9*, 1057.
 [39] J. Cheng, W. Ding, Y. Zi, Y. Lu, L. Ji, F. Liu, C. Wu, Z. L. Wang, *Nat. Commun.* **2018**, *9*, 3733.
 [40] Y. Chen, Y. Cheng, Y. Jie, X. Cao, N. Wang, Z. L. Wang, *Energy Environ. Sci.* **2019**, *12*, 2678.
 [41] V. Vivekananthan, W. J. Kim, N. R. Alluri, Y. Purusothaman, K. S. Abisegapriyan, S.-J. Kim, *Micro Nano Syst. Lett.* **2019**, *7*, 14.
 [42] L. Lin, Y. Xie, S. Niu, S. Wang, P. K. Yang, Z. L. Wang, *ACS Nano* **2015**, *9*, 922.
 [43] S. Li, S. Wang, Y. Zi, Z. Wen, L. Lin, G. Zhang, Z. L. Wang, *ACS Nano* **2015**, *9*, 7479.